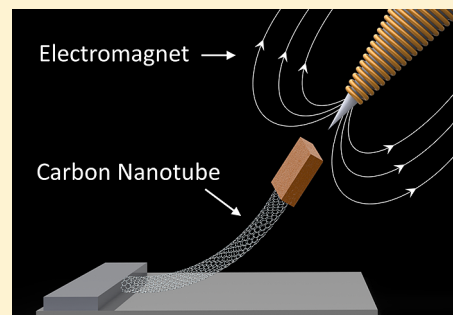


Magnetically Actuated Single-Walled Carbon Nanotubes

Samantha P. Roberts,^{*,†} Arthur W. Barnard,[‡] Christopher M. Martin,[§] Melina K. Bles,[†] Jonathan S. Alden,[‡] Alexander R. Ruyack,[§] and Paul L. McEuen^{*,†,||}

[†]Department of Physics, [‡]School of Applied and Engineering Physics, [§]Laboratory of Atomic and Solid State Physics, and ^{||}Kavli Institute for Nanoscale Science, Cornell University, Ithaca, New York 14853, United States

ABSTRACT: We couple magnetic tweezer techniques with standard lithography methods to make magnetically actuated single-walled carbon nanotube (SWNT) devices. Parallel arrays of 4–10 μm -long SWNT cantilevers are patterned with one end anchored to the substrate and the other end attached to a micron-scale iron magnetic tag that is free to move in solution. Thermal fluctuations of this tag provide a direct measurement of the spring constant of the SWNT cantilevers, yielding values of 10^{-7} – 10^{-8} N/m. This tag is also a handle for applying forces and torques using externally applied magnetic field gradients. These techniques provide a platform on which interaction forces between SWNTs and other objects such as biomolecules and cells can be measured *in situ*.



KEYWORDS: Single-walled carbon nanotubes, magnetic tweezers, carbon nanotube spring constant, magnetic force spectroscopy

Single walled carbon nanotubes (SWNTs) have remarkable mechanical, electrical, and optical properties.^{1–3} Cantilevers made from SWNTs have exhibited exceptional mass and force detection sensitivity,^{4,5} and applications as noninvasive cellular probes have been proposed.^{6–8}

Our current understanding of SWNT mechanics comes from attaching SWNTs to atomic force microscopy (AFM) tips and making direct force measurements^{9–12} or by exploring their uses in mechanical resonator devices.^{13–15} However, progress has been hampered with one-at-a-time device fabrication,¹⁶ the inability to exert arbitrary controlled forces and torques on the SWNTs, and the challenges of imaging them *in situ*.^{17–19}

Magnetic tweezers offer a way to address these challenges. For over two decades they have been used to explore the mechanical and structural properties of flexible biopolymers such as DNA.^{20,21} In these experiments a molecule is chemically tethered to a substrate while its free end is functionalized with a micron-scale magnetic bead. The bead makes the motion of the tethered molecule visible and serves as a handle to apply forces and torques via an external magnetic field gradient. Video analysis of the amplitude of thermal fluctuations $\langle \delta x^2 \rangle$ can be used to find the effective spring constant k of the molecule via the equipartition theorem:²²

$$k = \frac{k_B T}{\langle \delta x^2 \rangle} \quad (1)$$

Here we report the use of magnetic tweezer techniques to explore the properties of individual SWNTs. We measure the elastic spring constant of micron-length SWNTs, tune this spring constant using magnetic forces, and apply torque to the tubes. The measurement and manipulation of nanotubes using magnetic tweezers is applicable to studies of SWNTs in solution and opens up new possibilities for biological experiments *in situ*.

Fabrication and Measurement Techniques. We grow SWNTs on quartz substrates via chemical vapor deposition (CVD), as discussed in refs 23 and 24. The NTs grow with their long axis preferentially aligned to the crystalline orientation of the substrate. Atomic force microscope (AFM) and scanning electron microscope (SEM) images of a typical NT growth are shown in Figure 1a,b. We find the density of SWNTs to be 1–2 NTs/ μm with diameters that range from 0.6 to 4.0 nm. The device geometry, prior to being placed in liquid, is illustrated in Figure 1c, and optical images of completed devices are shown in Figure 1d,e. The starting substrate is a 170 μm -thick transparent fused silica wafer onto which a 50 nm poly silicon release layer (p-Si) is deposited via plasma-enhanced CVD. Regions of the p-Si where the NT is to be anchored to the substrate are then removed by reactive-ion etching. Nanotubes are then transferred from the quartz growth substrate to the device substrates using a 50 nm thin polymethyl-methacrylate (PMMA) mediator layer (methods modified from ref 25) and oriented such that their length is roughly perpendicular to the anchor contacts. The PMMA layer is removed with organic solvent, leaving behind the aligned SWNTs. Anchor contacts made of 2 nm/40 nm titanium/platinum tether the SWNTs to the fused silica. Micron-scale 150 nm-thick islands of iron are patterned in square, rectangular, and triangular shapes, spaced such that adjacent devices cannot make contact with each other. The NTs are cut to predefined lengths by an oxygen plasma using photoresist to protect the NTs in the regions between the tag and the contact.

The iron tags are released from the substrate by immersing the chip in a 1 molar bath of potassium-hydroxide (KOH) at

Received: April 9, 2015

Revised: July 24, 2015

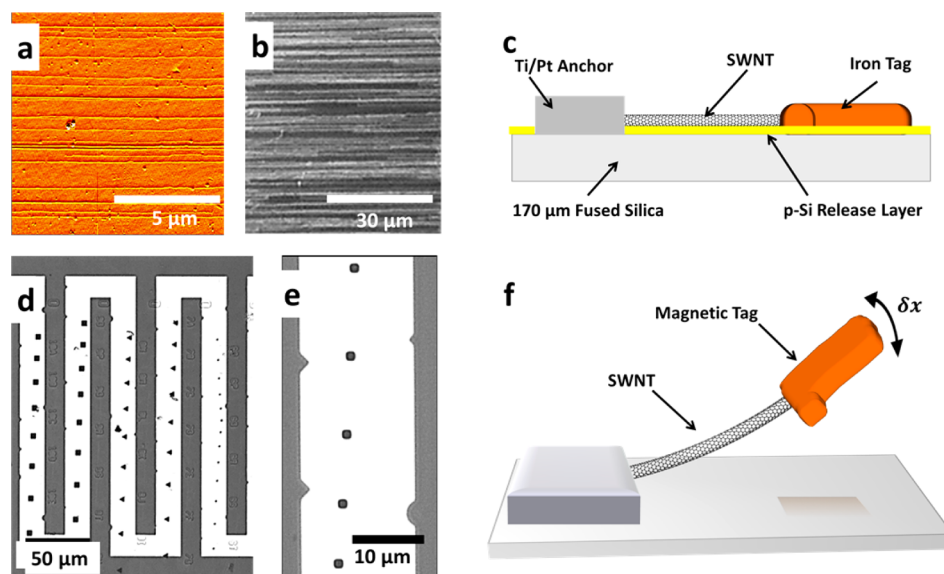


Figure 1. (a) AFM and (b) SEM images of aligned SWNTs on a quartz growth substrate. (c) Schematic of lithography layers of a magnetically tagged SWNT device. (d) Optical image of an array showing ~ 50 devices. Magnetic tags (dark squares, triangles) are tethered to interdigitated anchor lines (dark gray). (e) High magnification optical image of square iron tags at various distances from the contact. (f) Schematic of a magnetically tagged and tethered SWNT after etching the p-Si release layer in KOH. The iron tag shown has a symmetry breaking tab.

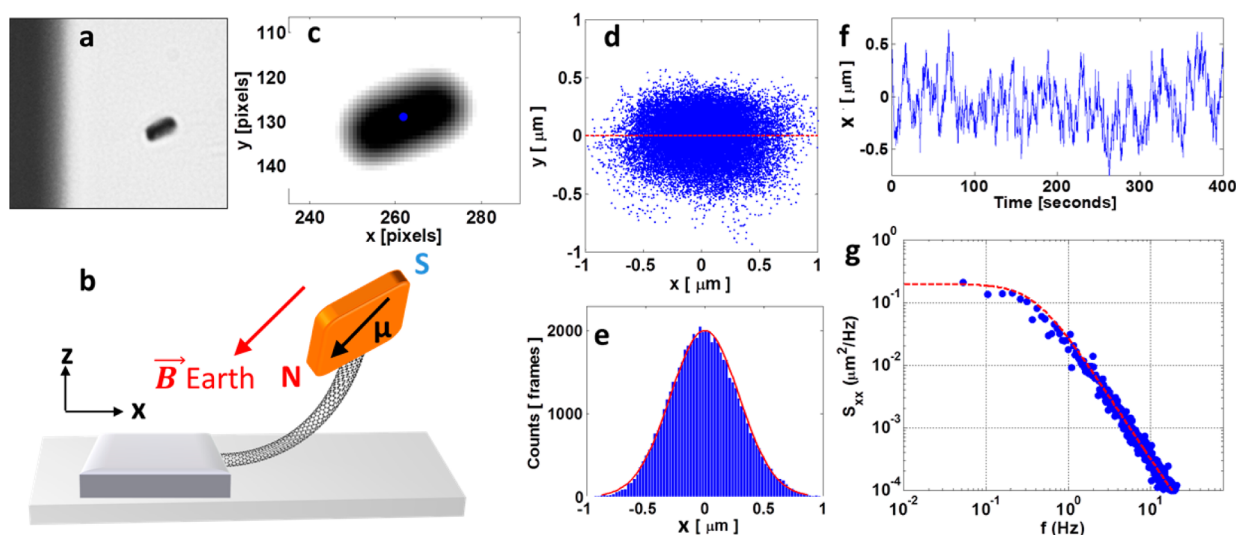


Figure 2. (a) Single frame of raw video data showing a 2- μm -square iron tag attached to the vertical anchor contact bar (dark region left side of image). The SWNT connecting the tag to the anchor is not visible. (b) Schematic of a SWNT with iron tag oriented with its magnetic moment (along its diagonal) aligned with the earth's magnetic field. (c) Image of the frame in (a) after image processing. The centroid of the pad is denoted by the blue dot. (d) Centroid positions in the x - y plane over 40,000 video frames centered about its mean position. (e) Histogram of fluctuations in x with $\sigma = 290$ nm. (f) Time trace of the centroid for 400 s. (g) Power spectral density over 60,000 video frames with a corner frequency of 0.3 Hz.

room temperature for 4–6 h to etch the p-Si from under the SWNTs and tags. The chip is then gently brought through several water baths to rinse and remains in water throughout the experiments. Iron tags that are not anchored by a connecting NT will freely diffuse through the water and are removed before experiment by passing a permanent magnet through the fluid, leaving behind only anchored NT devices. [Figure 1f](#) illustrates an iron tag released from the substrate, held by a connecting SWNT.

Measurements are performed using an inverted Olympus IX-71 microscope. The sample is mounted to a nonmagnetic brass stage plate via a thin wax layer, which serves as a hydrophobic barrier to keep water corralled on the top of the chip.

Micrometer adjustments at opposing corners of the stage prevent drift. Illumination from a halogen lamp is focused through a 0.55 numerical aperture (NA) condenser and passes through the device sample. Bright field images are collected via a 60 \times water immersion objective with a NA of 1.2. Focus height is changed via a computer controlled piezo-actuated z -stage (Piezo-Jena). The image passes through a 2 \times expander for enhanced resolution and is projected onto the progressive-scan Sony XCD-V60 video camera CCD array. Video images are acquired at 100–150 frames/second with a shutter speed of 5–10 ms.

[Figure 2a–g](#) shows measurements on an 8- μm -long SWNT device. A single frame from the video is seen in [Figure 2a](#), with

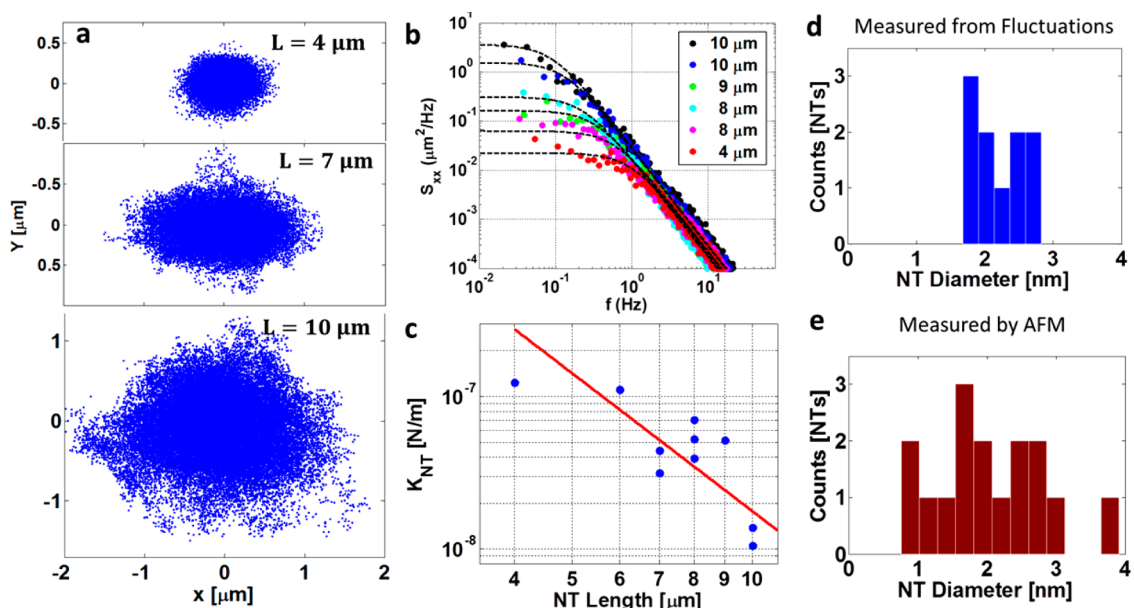


Figure 3. (a) Plots of the centroid position in the x – y plane for three devices of different lengths. The x and y axes have the same scales. The fluctuation amplitude increases for longer length SWNTs. (b) Power spectral density functions for seven devices with the same triangular iron tags. The integrated area of the PSD decreases as SWNT length decreases. (c) Spring constant vs SWNT length on a log–log scale where the red line is a plot of eq 4 for a SWNT with a diameter $d = 2.2$ nm. (d) Nanotube diameters predicted by beam mechanics given the spring constants in (c). (e) AFM measurements of NT diameters for a representative sample of NTs used to fabricate our devices.

the $2\text{-}\mu\text{m}$ -square iron pad at the center. The anchor contact is the dark vertical bar on the left side of the image, which also acts as a fiducial marker. By varying the focus, we find that the tag is several microns above the surface and is oriented on-edge. This is due to the fixed magnetic moment of the iron tag aligning to the earth's magnetic field as illustrated in Figure 2b.

Standard algorithms are used to find the centroid of the tag with subpixel resolution. A background-subtracted, thresholded image with Gaussian-blurred pixel intensities can be seen in Figure 2c, where the blue dot represents the centroid of the iron tag for the video frame in Figure 2a. We find that we have 10 nm resolution in determining the centroid of the tag. Figure 2d shows the centroid position for 40,000 video frames in the x – y plane centered about its mean position, where x is taken to be the principal axis along which maximal average displacements are measured. We note the area traversed is elliptical with a directional preference that is unique for each device. The fluctuations in x are seen in the histogram in Figure 2d and are normally distributed (red fit) with a standard deviation σ of 290 nm for this device.

The power spectral density (PSD) of the fluctuations over time in Figure 2f is shown in Figure 2g on a log–log scale denoted S_{xx} . The red line is a fit to the theoretical one-sided PSD for Brownian thermal motion:²⁶

$$S_{xx} = \frac{D}{\pi^2(f^2 + f_c^2)} \quad (2)$$

We see this device has a corner frequency of $f_c \approx 0.3$ Hz. Integrating the area under the PSD curve gives the RMS fluctuations $\langle \delta x^2 \rangle$. Using eq 1 we calculate the NT spring constant and find $k_{NT} = 4.7 \times 10^{-8}$ N/m. We determine the diffusion constant D from the PSD fit to be $0.17 \mu\text{m}^2/\text{s}$. Modeling the tag as a thin disk,²⁷ we infer the mean effective radius given by the Stokes–Einstein relation:

$$R_{eff} = \frac{k_B T}{6\pi\eta D} = (1/2)a + (\pi/4)b \quad (3)$$

Here $a = 150$ nm is the thickness of the iron tag, b is the effective tag radius, and η is the viscosity of water at room temperature. We find a radius of $b = 1.4 \mu\text{m}$, which is consistent with the $2 \times 2 \mu\text{m}^2$ tag size.

The centroid distributions for 4, 7, and $10 \mu\text{m}$ long NTs are shown in Figure 3a. Longer NTs have larger fluctuation amplitudes, with lower corner frequencies as seen in the PSDs of Figure 3b. Figure 3c shows the spring constant as a function of NT length on a log–log scale. The stiffest NT is the shortest, with a spring constant of 1.1×10^{-7} N/m, while the longest device of $10 \mu\text{m}$ has the softest spring constant, 1.4×10^{-8} N/m.

To understand these results, we model the SWNT as a thin-walled hollow cylindrical beam of average diameter d with length L , yielding a spring constant:²⁸

$$k_{NT} = \frac{\beta_0^4 E t \pi d^3}{8L^3} \quad (4)$$

Here the Young's modulus, $E = 1$ TPa, and t is the sidewall thickness of the SWNT taken to be 0.34 nm. The coefficient $\beta_0 = 1.88$ corresponds to the boundary conditions for the fundamental bending mode. This predicts a $1/L^3$ dependence, as shown by the red line in Figure 3c for a nanotube of diameter $d = 2.2$ nm. Combining eq 1 with eq 4 we find the NT inferred diameter for each tube:

$$d_{NT} = \left(\frac{8k_B T L^3}{\beta_0^4 E t \pi \delta x^2} \right)^{1/3} \quad (5)$$

We find $1.6 \text{ nm} \leq d_{NT} \leq 2.8 \text{ nm}$ with a mean diameter of 2.2 nm. A histogram can be seen in Figure 3d in blue. For comparison, AFM height data of a representative SWNT

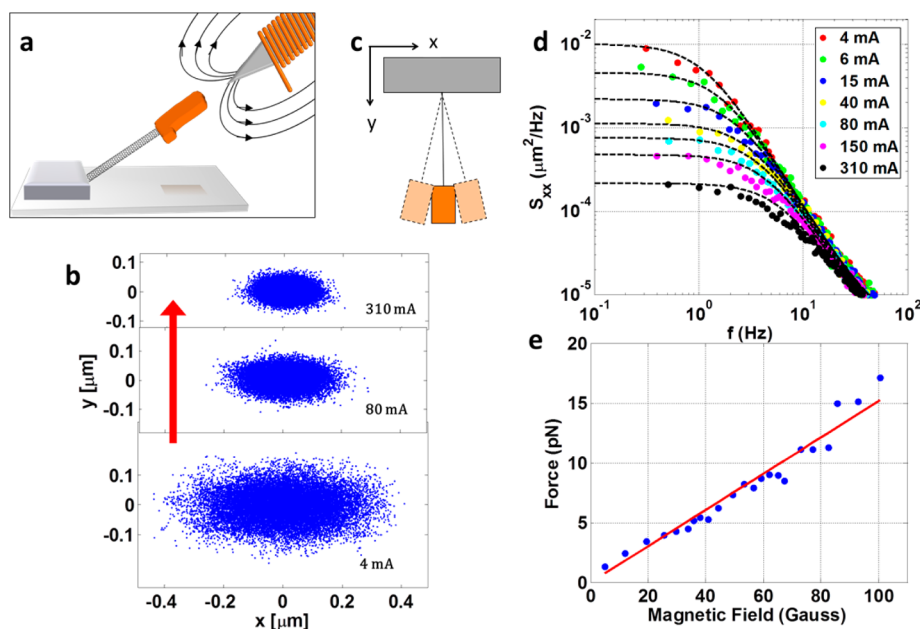


Figure 4. (a) Schematic of a magnetically tensioned SWNT. Black arrows denote magnetic field lines. (b) Centroid position in the x - y plane for three different values of solenoid current. The x and y axes have the same scale. Red arrow indicates direction of increased tension. (c) Top down view of the device with the principal axis of motion measured denoted by x . (d) PSDs of the centroid fluctuations. (e) Tensioning force as a function of magnetic field. The red line is a linear fit.

growth is seen in Figure 3e in red. We see that diameters derived from our fluctuation measurements are consistent with the typical diameters of NTs used to make the devices.

These SWNTs have extremely soft springs constants with values a million times softer than the softest AFM imaging tips. This feature means that SWNTs will experience large deflections for a small applied transverse force and thus can be utilized for ultrasensitive force detection. The force sensitivity of our devices is limited by the thermal noise due to Brownian forces:²⁶

$$\delta F = \sqrt{4k_B T \gamma \Delta f} \quad (6)$$

Here $\gamma = k_B T / D$ is the friction coefficient and Δf is the bandwidth. As the diffusion coefficient D is set by the size of the iron tag, the force sensitivity stays a constant 40 fN/ $\sqrt{\text{Hz}}$ for all device lengths. However, longer NTs will display larger displacements than shorter NTs for the same applied force, making them easier to detect.

Tensioning SWNTs. We now look at fluctuations while the NT is being tensioned along its axis by a magnetic field B . The tensioning force on an iron tag with magnetic moment μ is proportional to the field gradient generated by the magnet:

$$F_{\text{mag}} = \mu \left(\frac{\partial B}{\partial r} \right) \quad (7)$$

To apply this force we use an electromagnet made of 32 gauge magnet wire wound along an aluminum spindle. Its core is filled with a 500- μm -diameter Permalloy-80 wire, a ferromagnetic alloy with very low hysteresis.^{29,30} The wire is sharpened to a 50 μm point by hand lapping on fine grit sandpaper. The point is positioned so it extended out 3 mm from the end of the solenoid coil, as is illustrated in Figure 4a. The electromagnet is mounted onto a 3-axis piezo nanomanipulator (Patch-Star), and current to the electromagnet is varied via a computer-controlled digital-to-analog converter.

Figure 4 shows measurements of a 10 μm long SWNT with a 2 $\mu\text{m} \times 3 \mu\text{m}$ rectangular iron tag in a magnetic field gradient. The magnet is placed with its tip directly in the water positioned 120 μm away from the device and the magnet axis made an angle of 30 degrees with respect to the horizontal (Figure 4a). Current through the magnet is stepped from 4 to 310 mA over 22 steps, while the tag position was tracked as above. Figure 4b shows centroid distributions for three current values. The highest-amplitude fluctuations preferentially occur perpendicular to the tensioned NT axis, as illustrated schematically in Figure 4c. Increased solenoid current causes decreased fluctuation amplitudes and increased corner frequencies as shown in the PSDs in Figure 4d. (Note: the fluctuations in y are predominantly the projection of motion perpendicular to the nanotube axis onto the imaging plane.)

This magnetic tensioning pulls the CNT taut and creates an additional contribution to the transverse spring constant F_{mag}/L . At large tensions, we can equate this to the experimentally measured spring constant $k_B T / \delta x^2$ to directly probe F_{mag} without any need for calibration of the magnetic gradients. We plot the tension force as a function of magnetic field for each of the currents measured in Figure 4e. The tension varies linearly with the magnetic field between 0 and 20 pN, as illustrated by the red fit. From eq 7 the slope of this line gives the magnetic moment μ of the tag, from which we infer $\mu = 1.3 \times 10^{-12}$ J/T. We compare this to the saturated magnetic moment of the tag $\mu_{\text{sat}} = 1.6 \times 10^{-12}$ J/T, which is in close agreement.

When the magnetic field is removed the tag returns to its original position, and a measurement of the spring constant reveals the NTs untensioned spring constant. We can thus reversibly control and measure the tension in the nanotube over a broad range of parameters using these magnetic tweezers.

Bending and Twisting SWNTs. To exert torsional forces on the SWNT we use a two-magnet geometry illustrated

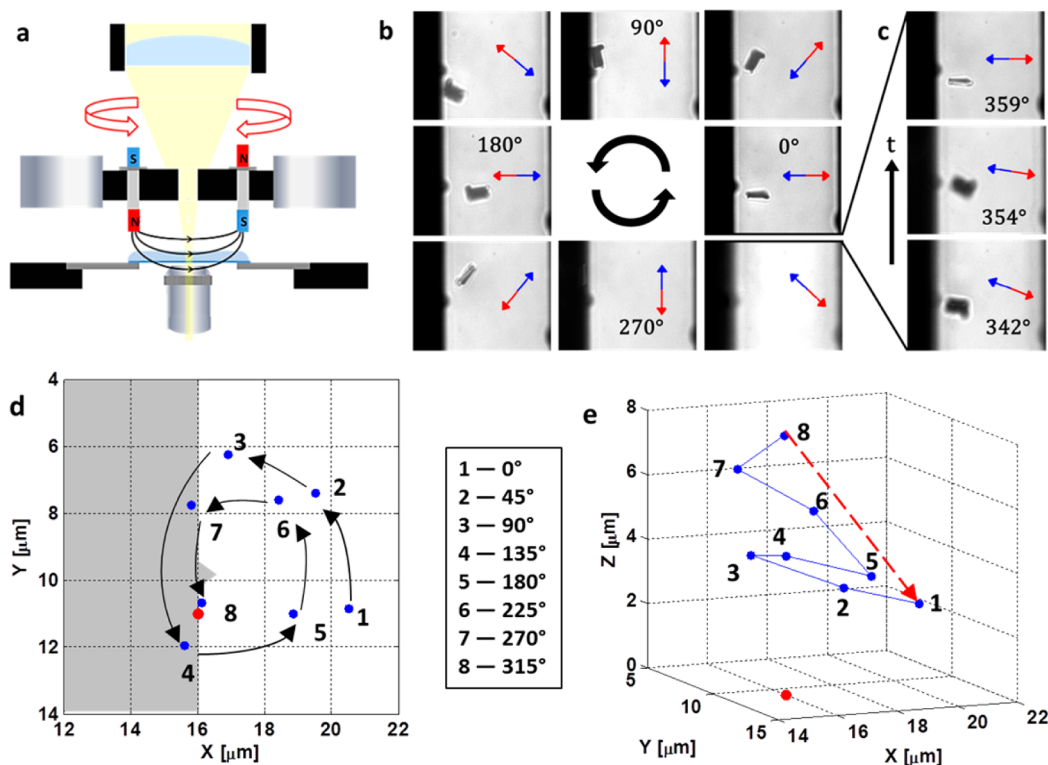


Figure 5. (a) Magnet geometry for rotation experiments. North and south poles are red and blue, respectively. (b) Eight video frames during a 360° rotation of the magnets. We see a rectangular tag with a symmetry breaking marker at one corner. The arrows represent the direction of the magnetic field (with red pointing to the north magnet and blue pointing toward the south magnet). The magnetic tag aligns and rotates with the magnetic field until $\sim 340^\circ$ when the SWNT untwists in two successive flips about its long axis as seen in (c). The tag is above the anchor contact (dark vertical bar) and only faintly visible in images between 270° and 340° . (d,e) NT motion in (b). The red dot is where the NT is held by the anchor contact (gray), and the blue dots are where the NT attaches to the iron tag at each position. (d) Decreasing radius with increased rotation in the x - y plane, which corresponds to an increase in height off the substrate as illustrated in (e). The red dashed line in (e) represents the untwisting of the NT, returning to its original position.

schematically in Figure 5a. Here two permanent neodymium magnets are mounted onto a remotely controlled rotation stage and centered 2 mm above the sample, with opposite poles separated by 20 mm. This creates a constant magnetic field parallel to the image plane with a vertical force gradient of ~ 0.1 T/m.

Figure 5b,c shows video images of a $2 \mu\text{m} \times 3 \mu\text{m}$ iron tag with a symmetry-breaking tab, attached to a $10\text{-}\mu\text{m}$ -long SWNT. Video frames are shown starting at (an arbitrarily chosen) 0° for one 360° counterclockwise rotation of the magnets at $5^\circ/\text{s}$, while the focus was manually varied to track the tag during rotation. The direction of the magnetic field is represented by the blue (south pole) and red (north pole) arrows in each video frame. We see that the tag orients and rotates with its long axis parallel to the magnetic field. From 270° to 340° the tag is not easily visible as it is over the anchor contact (dark vertical bar, left side). Between 340° and 360° we observe (Figure 5c, from bottom to top) the pad untwists with two successive 180° flips about its axis, while the tag maintained alignment with the magnetic field. At 360° of magnet rotation the iron tag is back in its original 0° position.

Figure 5d illustrates the rotation of the free end of the NT at each of the positions in Figure 5b. The red dot is the NT anchor point, and the blue dots show the attachment point of the NT to the iron tag. We see that the NT is rotated in a circular path around the anchor point. The NT must accommodate this rotation by either bending or twisting or a combination of both. Figure 5e shows the same data as in

Figure 5d but with the focal height (z) above the substrate at each of the eight positions. We see that as the rotation increases the NT is elongated off the substrate and pulled to more than $3/4$ of its length at 315° (#8). At greater rotations the NT relieves this rotational stress by untwisting (as shown in Figure 5c), and returns to its original position (#1), a transition that is illustrated in Figure 5e by the red dashed line.

This untwisting behavior is observable for repeated rotations and occurs at the same angle ($\sim 340^\circ$) for this device. These data show the competition between the magnetic force, which rotates the iron tag, and the elastic restoring force of the SWNT, which resists this motion. Additionally, this illustrates the resiliency of CNTs as they return to their original state even after repeated bending and twisting deformations.

There is significant interest in the mechanical behavior of SWNTs as they undergo torsional forces, and many nonlinear effects such as buckling and NT sidewall collapse are predicted by simulations.^{31,32} With modification to the magnet geometry to increase the field gradient, this magnetic tweezer platform serves as a potential way to measure these transitions.

Conclusions and Future Work. We have for the first time used magnetic tweezers to measure the fundamental mechanical properties of SWNTs in solution and used these tweezers to apply well-defined forces and torques. Our system allows *in situ* measurement of the properties of individual nanotubes. It also opens the door to new kinds of experiments that explore the interaction of SWNTs with biological molecules or cells, a

topic of great interest for the use of SWNTs in medical applications.^{33–35}

AUTHOR INFORMATION

Corresponding Authors

*E-mail: spr26@cornell.edu.

*E-mail: plm23@cornell.edu.

Notes

The authors declare no competing financial interest.

ACKNOWLEDGMENTS

This work was supported by the Cornell Center for Materials Research (National Science Foundation (NSF) grant DMR-1120296), the Air Force Office of Scientific Research (FA9950-10-1-0410), the Office of Naval Research (FA9550-09-1-0705), and NSF (grant 0928552). Devices were fabricated at the Cornell Nanoscale Science and Technology Facility, which is supported by the National Science Foundation (NSF) (ECCS-0335765). We thank Anthony Traglia for helpful conversations and writing the magnet-rotation control code.

REFERENCES

- (1) Qian, D.; Wagner, G. J.; Liu, W. K.; Yu, M.-F.; Ruoff, R. S. Mechanics of Carbon Nanotubes. *Appl. Mech. Rev.* **2002**, *55*, 495–533.
- (2) McEuen, P. L.; Park, J.-Y. Electron Transport in Single-Walled Carbon Nanotubes. *MRS Bull.* **2004**, *29*, 272–275.
- (3) Avouris, P. Carbon Nanotube Photonics and Optoelectronics. *Nat. Photonics* **2008**, *2*, 341–350.
- (4) Feng, E. H.; Jones, R. E. Carbon Nanotube Cantilevers for next-Generation Sensors. *Phys. Rev. B: Condens. Matter Mater. Phys.* **2011**, *83*, 195412.
- (5) Jensen, K.; Kim, K.; Zettl, A. An Atomic-Resolution Nano-mechanical Mass Sensor. *Nat. Nanotechnol.* **2008**, *3*, 533–537.
- (6) Kam, N. W. S.; Liu, Z.; Dai, H. Carbon Nanotubes as Intracellular Transporters for Proteins and DNA: An Investigation of the Uptake Mechanism and Pathway. *Angew. Chem., Int. Ed.* **2006**, *45*, 577–581.
- (7) Yang, W.; Thordarson, P.; Gooding, J. J.; Ringer, S. P.; Braet, F. Carbon Nanotubes for Biological and Biomedical Applications. *Nanotechnology* **2007**, *18*, 412001.
- (8) Chen, X.; Kis, A.; Zettl, A.; Bertozzi, C. R. A Cell Nanoinjector Based on Carbon Nanotubes. *Proc. Natl. Acad. Sci. U. S. A.* **2007**, *104*, 8218–8222.
- (9) Hafner, J. H.; Cheung, C. L.; Lieber, C. M. Direct Growth of Single-Walled Carbon Nanotube Scanning Probe Microscopy Tips. *J. Am. Chem. Soc.* **1999**, *121*, 9750–9751.
- (10) Wilson, N. R.; Macpherson, J. V. Carbon Nanotube Tips for Atomic Force Microscopy. *Nat. Nanotechnol.* **2009**, *4*, 483–491.
- (11) Snow, E. S.; Campbell, P. M.; Novak, J. P. Single-Wall Carbon Nanotube Atomic Force Microscope Probes. *Appl. Phys. Lett.* **2002**, *80*, 2002–2004.
- (12) Bunch, J. S.; Rhodin, T. N.; McEuen, P. L. Noncontact-AFM Imaging of Molecular Surfaces Using Single-Wall Carbon Nanotube Technology. *Nanotechnology* **2004**, *15*, S76–S78.
- (13) Nishio, M.; Sawaya, S.; Akita, S.; Nakayama, Y. Carbon Nanotube Oscillators toward Zeptogram Detection. *Appl. Phys. Lett.* **2005**, *86*, 133111.
- (14) Sazonova, V.; Yaish, Y.; Üstünel, H.; Roundy, D.; Arias, T. A.; McEuen, P. L. A Tunable Carbon Nanotube Electromechanical Oscillator. *Nature* **2004**, *431*, 284–287.
- (15) Barnard, A. W.; Sazonova, V.; van der Zande, A. M.; McEuen, P. L. Fluctuation Broadening in Carbon Nanotube Resonators. *Proc. Natl. Acad. Sci. U. S. A.* **2012**, *109*, 19093–19096.
- (16) Martinez, J.; Yuzvinsky, T. D.; Fennimore, A. M.; Zettl, A.; García, R.; Bustamante, C. Length Control and Sharpening of Atomic Force Microscope Carbon Nanotube Tips Assisted by an Electron Beam. *Nanotechnology* **2005**, *16*, 2493–2496.
- (17) Troiani, H. E.; Miki-Yoshida, M.; Camacho-Bragado, G. A.; Marques, M. A. L.; Rubio, A.; Ascencio, J. A.; Jose-Yacamán, M. Direct Observation of the Mechanical Properties of Single-Walled Carbon Nanotubes and Their Junctions at the Atomic Level. *Nano Lett.* **2003**, *3*, 751–755.
- (18) Iijima, S.; Brabec, C.; Maiti, A.; Bernholc, J. Structural Flexibility of Carbon Nanotubes. *J. Chem. Phys.* **1996**, *104*, 2089–2092.
- (19) Fakhri, N.; Tsybouski, D. A.; Cognet, L.; Weisman, R. B.; Pasquali, M. Diameter-Dependent Bending Dynamics of Single-Walled Carbon Nanotubes in Liquids. *Proc. Natl. Acad. Sci. U. S. A.* **2009**, *106*, 14219–14223.
- (20) Bustamante, C.; Bryant, Z.; Smith, S. B. Ten Years of Tension: Single-Molecule DNA Mechanics. *Nature* **2003**, *421*, 423–427.
- (21) De Vlaminck, I.; Dekker, C. Recent Advances in Magnetic Tweezers. *Annu. Rev. Biophys.* **2012**, *41*, 453–472.
- (22) Lionnet, T.; Allemand, J.-F.; Revyakin, A.; Strick, T. R.; Saleh, O. A.; Bensimon, D.; Croquette, V. Single-Molecule Studies Using Magnetic Traps. *Cold Spring Harb. Protoc.* **2012**, *1*, 34–49.
- (23) Ding, L.; Yuan, D.; Liu, J. Growth of High-Density Parallel Arrays of Long Single-Walled Carbon Nanotubes on Quartz Substrates. *J. Am. Chem. Soc.* **2008**, *130*, 5428–5429.
- (24) Kocabas, C.; Hur, S.-H.; Gaur, A.; Meitl, M. A.; Shim, M.; Rogers, J. A. Guided Growth of Large-Scale, Horizontally Aligned Arrays of Single-Walled Carbon Nanotubes and Their Use in Thin-Film Transistors. *Small* **2005**, *1*, 1110–1116.
- (25) Jiao, L.; Fan, B.; Xian, X.; Wu, Z.; Zhang, J.; Liu, Z. Creation of Nanostructures with Poly(methyl Methacrylate)-Mediated Nanotransfer Printing. *J. Am. Chem. Soc.* **2008**, *130*, 12612–12613.
- (26) De Groot, B. G. A Simple Model for Brownian Motion Leading to the Langevin Equation. *Am. J. Phys.* **1999**, *67*, 1248–1252.
- (27) Jennings, B. R.; Parslow, K. Particle Size Measurement: The Equivalent Spherical Diameter. *Proc. R. Soc. London, Ser. A* **1988**, *419*, 137–149.
- (28) Li, C.; Chou, T.-W. A Structural Mechanics Approach for the Analysis of Carbon Nanotubes. *Int. J. Solids Struct.* **2003**, *40*, 2487–2499.
- (29) Yapici, M. K.; Zou, J. Permalloy-Coated Tungsten Probe for Magnetic Manipulation of Micro Droplets. *Microsyst. Technol.* **2008**, *14*, 881–891.
- (30) Boothby, O. L.; Bozorth, R. M. A New Magnetic Material of High Permeability. *J. Appl. Phys.* **1947**, *18*, 173–176.
- (31) Yakobson, B. I.; Brabec, C. J.; Bernholc, J. Nanomechanics of Carbon Tubes: Instabilities beyond Linear Response. *Phys. Rev. Lett.* **1996**, *76*, 2511–2514.
- (32) Rochefort, A.; Avouris, P.; Lesage, F.; Salahub, D. R. Electrical and Mechanical Properties of Distorted Carbon Nanotubes. *Phys. Rev. B: Condens. Matter Mater. Phys.* **1999**, *60*, 13824–13830.
- (33) Klingeler, R.; Sim, R. B., Eds. *Carbon Nanotubes for Biomedical Applications*; Springer: Berlin, Heidelberg, 2011.
- (34) Heister, E.; Brunner, E. W.; Dieckmann, G. R.; Jurewicz, I.; Dalton, A. B. Are Carbon Nanotubes a Natural Solution? Applications in Biology and Medicine. *ACS Appl. Mater. Interfaces* **2013**, *5*, 1870–1891.
- (35) He, H.; Pham-Huy, L. A.; Dramou, P.; Xiao, D.; Zuo, P.; Pham-Huy, C. Carbon Nanotubes: Applications in Pharmacy and Medicine. *BioMed Res. Int.* **2013**, *2013*, 1–12.